# Fokker-Planck simulations of short-pulse-laser–solid experiments

R. P. J. Town and A. R. Bell
*Blackett Laboratory, Imperial College of Science, Technology and Medicine, London SW7 2BZ, United Kingdom*

S. J. Rose
*Rutherford Appleton Laboratory, Chilton, Didcot, Oxfordshire OX11 0QX, United Kingdom*
*and Department of Physics and Space Science, University of Birmingham, Birmingham, B15 2TT, United Kingdom*
(Received 25 February 1994)

This paper describes simulations of short-pulse-laser–solid experiments using a one-dimensional Fokker-Planck code. Results are presented which show that the Spitzer theory of heat flow is inapplicable for these experiments. The ionization dynamics have been investigated by post-processing using an average atom model. It is found that the dominant processes are collisional ionization and three-body recombination and that full ionization takes a significant fraction of the rise time of the laser pulse. The collisional ionization rates obtained from a Maxwellian distribution are found to be in good agreement with those obtained from convolving the cross sections with the actual distribution.

PACS number(s): 52.25.Jm, 52.50.Jm, 52.65.+z

## I. INTRODUCTION

The development of short-pulse high-intensity lasers has opened up an exciting new regime in the study of laser-produced plasmas. These lasers can produce intensities on target in the range $10^{15}$–$10^{18}$ W/cm$^2$ in pulse lengths of less than a picosecond. The brevity of the pulse leads to density scale lengths that are typically less than 0.5 micrometers.

Unlike the long-pulse lasers used in the inertial confinement fusion experiments such short laser pulses do not interact with a long density scale length, subcritical plasma corona. The energy is absorbed in a narrow skin layer that is rapidly heated to a temperature exceeding 1 keV. This heat front has little time to penetrate into the solid target, so the temperature scale length is of the same order as the density scale length, i.e., submicrometer.

Thus the interaction of a short-pulse laser with a solid target generates a solid density, keV plasma. At keV temperatures and densities the electron mean free path of the thermal electrons is approximately 0.05 $\mu$m. The scale lengths and the mean free path are, therefore, of the same order. Hence we would expect the heat flow to be poorly approximated by the classical Spitzer-Härm theory of heat transport [1] and for the electron distribution function to be strongly non-Maxwellian.

During the short-pulse interaction an initially cold, unionized solid is rapidly heated to a hot, ionized solid density plasma. Ionization is, thus, an important mechanism in the time development of the plasma.

In this paper we will look at the intermediate intensity regime ($10^{15}$ W/cm$^2$) where relativistic effects are not important. This regime is especially important for the generation of short-pulse x-ray lasers by the recombination scheme [2]. We will look in detail at the non-Maxwellian character of the electron distribution function and how it affects the heat transport and the ionization rates.

In Sec. II we outline the Fokker-Planck (FP) code that has been used to simulate the interaction of a short-pulse laser with a solid target. We also briefly present a description of the ionization dynamics model [3] which postprocesses the density and temperature to predict the ionization state as a function of time.

Section III presents results from the FP code and compares them with similar simulations using a hydrodynamic code with Spitzer conductivity. Results showing the ionization state as a function of time are presented in Sec. IV. Section V compares the collisional ionization rates obtained using the actual distribution obtained from the FP code with that obtained from a Maxwellian distribution of the same density and temperature. Finally Sec. VI draws conclusions and outlines future work.

## II. DESCRIPTION OF THE MODELS

The FP code has one spatial dimension and uses the diffusive approximation in which the distribution function, $f$, is written as

$$f(\vec{z},\vec{v}) = f_0(\vec{z},|\,\vec{v}\,|) + f_1(\vec{z},|\,\vec{v}\,|)\vec{v}/|\,\vec{v}\,|\,. \tag{1}$$

The diffusive approximation has been used successfully in previous calculations [4–7] and leads to a coupled set of equations for $f_0$ and $f_1$,

$$\frac{\partial f_0}{\partial t} + \frac{v}{3}\frac{\partial f_1}{\partial z} - \frac{v}{3}\frac{\partial U}{\partial z}\frac{\partial f_0}{\partial v} - \frac{\alpha}{3v^2}\frac{\partial}{\partial v}(v^2 f_1) = \frac{Y_{ee}}{3v^2}\frac{\partial}{\partial v}\left[3f_0 I_0^0 + v(I_2^0 + J_{-1}^0)\frac{\partial f_0}{\partial v}\right] \tag{2}$$

$$-\frac{(Z+1)n_e Y_{ee}}{v^3} f_1 = \frac{\partial f_1}{\partial t} + v\frac{\partial f_0}{\partial z} - \alpha\frac{\partial f_0}{\partial v} - \frac{2}{5}\frac{\partial U}{\partial z}\frac{\partial}{\partial v}(v f_1) - \frac{1}{5}\frac{\partial U}{\partial z} v\frac{\partial f_1}{\partial v}\,, \tag{3}$$

where

$$\alpha = \frac{e}{m_e}E, \qquad Y_{ee} = 4\pi\frac{e^2}{m_e}\ln\Lambda,$$
$$I_j^i = \frac{4\pi}{v^j}\int_0^v f_i u^{j+2}du \quad J_j^i = \frac{4\pi}{v^j}\int_v^\infty f_i u^{j+2}du. \tag{4}$$

The major advantages of this approximation is faster execution; less distribution function information has to be stored and the time step can exceed the collision time. However, the numerical solution of the diffusive approximation must be solved in an unconditionally stable manner for both the velocity and spatial differentials. The method of solution chosen is the alternating direction implicit scheme [8] which had been used successfully previously in one [7] and two spatial dimensions [9,10]. In this scheme during one time step the velocity differentials are treated implicitly and the spatial differentials are treated explicitly. The next time step the spatial differentials are treated implicitly and the velocity differentials are treated explicitly.

A number of approximations have been made to the coupled set of equations for $f_0$ and $f_1$. The Ohmic heating term in the $f_0$ equation, $\frac{\alpha}{3v^2}\frac{\partial}{\partial v}v^2 f_1$, has been neglected. In one dimension the electric field is obtained by the zero current condition, hence $\mathbf{J}\cdot\mathbf{E}$ is zero so there is no net heating and the $\frac{\alpha}{3v^2}\frac{\partial}{\partial v}v^2 f_1$ term serves only to transfer energy between electrons at different velocities. Epperlein has checked this approximation and found it to be valid in his simulations [11]. The $df_1/dt$ term in the $f_1$ equation has been ignored. This is valid provided that the collision time of the heat carrying electrons is short compared to the time scale of interest.

The FP equation is coupled to the ion hydrodynamic equations in Lagrangian form. However, the ion motion terms in the $f_1$ equation, but not in the $f_0$ equation, have been neglected. The laser energy is deposited using the collisional operator of Langdon [12]. The heat is supplied to the electrons in one of two ways, either by classical inverse bremsstrahlung, or by simply dumping the energy in a skin depth. The laser energy is thus taken up by the low-velocity electrons. However particle-in-cell (PIC) simulations [13] point to a collisionless absorption mechanism which leads to the generation of fast electrons. Such electrons are currently not included in the model.

The non-LTE (LTE is local thermodynamic equilibrium) ionization dynamics are followed by using an average atom model to follow the time evolution of the principal quantum shell occupancies averaged over the distribution of ionic states. The model is based on that developed by Lokke and Grasberger [14]. The model involves a series of coupled differential equations for the time evolution of the shell occupancies. The processes included are collisional excitation and ionization and their inverse process: collisional deexcitation and three-body recombination. Also included are the spontaneous bound-bound and free-bound radiative rates.

The model takes as its inputs the nuclear charge, atomic weight, and the time histories of the electron temperature, material density, and radiation temperature. It then outputs the time development of the population of each shell and the average ion state. The average-atom model has been more fully discussed in Ref. [3].

## III. RESULTS FROM THE FP CODE

Understanding the absorption process in subpicosecond laser–solid interaction is a major issue. Experiments have been performed with intensities above $10^{16}$ W/cm$^2$ which show an absorption fraction as high as 50% [15,16]. However, simulations with collisional absorption show an absorption fraction of only 10%. When we employed the classical inverse bremsstrahlung operator we obtained initially high absorption of laser energy which fell as time progressed (see Fig. 1). The inverse bremsstrahlung process scales as $n_e/T$. As time progresses the temperature increases and the density, due to hydrodynamic expansion, decreases. Hence the amount of absorption decreases. In order to get a level of absorbed energy consistent with experimental data we are dumping a fixed amount of energy in a skin depth. The energy is taken up by the low-velocity collisional electrons. Figure 1 shows the average absorption as a function of time for a typical run using classical inverse bremsstrahlung and a run with the same initial parameters using the energy absorbed in a skin depth.

Despite the short time scale of the interaction of the pulse with the target we have found that the ion hydrodynamics is significant. For example, Fig. 2 shows the density and temperature profiles at the peak of the pulse and at the end of the simulation. The initial conditions were as follows. A 0.4 $\mu$m thick fully ionized carbon ($Z = 6$) solid target was illuminated by a 350 fsec Gaussian KrF ($\lambda = 0.25$ $\mu$m) laser pulse. The target was initially at solid density ($n_e = 3.0 \times 10^{23}$ cm$^{-3}$) and at a temperature of 15 eV. A step profile was used between the target and the vacuum. A uniform velocity mesh with 70 grid points extending to a maximum velocity of 40 times the thermal velocity was used. A nonuniform spatial mesh

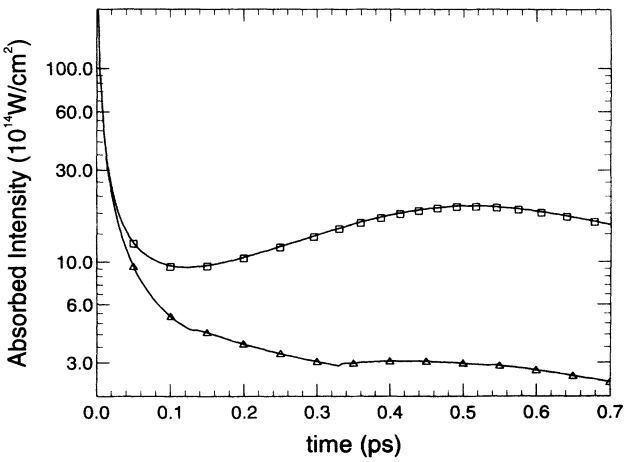


FIG. 1. Time averaged absorbed intensity as a function of time for classical inverse bremsstrahlung absorption (△) and forced energy dump (□).

with a minimum physical cell size of 0.002 $\mu$m was found to be necessary to model the hydrodynamic response. An average absorbed intensity of $8.0\times10^{14}$ W/cm$^2$ was used.

We can clearly see significant hydrodynamic motion. By the peak of the pulse a density scale length of approximately 0.28$\lambda$ has formed. At the end of the simulation a significant shelf of low density plasma has formed, with a scale length of 0.7$\lambda$. For these simulation parameters a critical surface has not formed. However, when the pulse length was increased to 0.5 psec and the absorbed intensity was fixed at $10^{15}$ W/cm$^2$ a critical surface had formed by the peak of the pulse. This suggests that the collisionless resonance absorption mechanism could play an important role in energy absorption. Collisionless PIC simulations with immobile ions have been performed [13] which have shown peak absorption of almost 80% at an incident angle of 50° with an irradiance of $10^{16}$ W/cm$^2\mu$m$^2$ and scale length of 0.1$\lambda$. These results have been modified when the ions are allowed to move. PIC simulations [17] now show the formation of an underdense shelf which has been found to enhance the absorption.

In long-pulse simulations the effects of a FP treatment of the heat flow has been successfully modeled using a flux limited Spitzer heat flow. This limits the heat flow to some fraction, $f$, of the free streaming limit. Experimental and simulation evidence in long-pulse interactions put the value of $f$ in the range 0.03–0.1. We have found that a flux limit of 0.1 is too low to reproduce the FP heat flow in the solid target. Figure 3 shows the spatial profiles of temperature (dotted line), FP heat flow (solid line), and the flux limited Spitzer heat flow (solid triangles) at the peak of the pulse. The Spitzer heat flow is calculated from the temperature profile and then limited to $f$=0.1 using the harmonic mean cutoff. As can be seen the flux limited Spitzer heat flow consistently underestimates the FP heat flow in the target and in the region of energy absorption.

Figure 4 shows the temperature, FP heat flow, and Spitzer heat flow limited to $f$=0.3. The flux limit of 0.3 gives a much better fit to the FP heat flow in the main body of the target. However, in the heated region the Spitzer heat flow overestimates the FP heat flow.

It is difficult to fix a flux limited Spitzer heat flow to the FP heat flow by a single value. However, it seems that in the bulk of the target $f$=0.3 is a reasonable approximation.

We have also compared the FP code with an unflux limited Spitzer hydrodynamic code. Figure 5 shows the temperature and heat flow profiles at the peak of the pulse for the Spitzer code (dotted line) and the FP code (solid line). The density profiles are very similar in both cases. There is a somewhat larger difference in the temperature and heat flow. The FP temperature has the characteristic "bent knee" profile around the energy absorption region. In this region the high-velocity electrons conduct the heat away whilst the low velocity electrons absorb the energy. In order to "pump" the conducting electrons there is a pool of relatively high velocity electrons that leads to a high temperature. Just outside the heated region the distribution is more Maxwellian and hence at a lower temperature. The Spitzer heat conduction takes no account of non-Maxwellian distribution effects and thus the temperature has a smooth convex profile. The heat flow is significantly different. The Spitzer

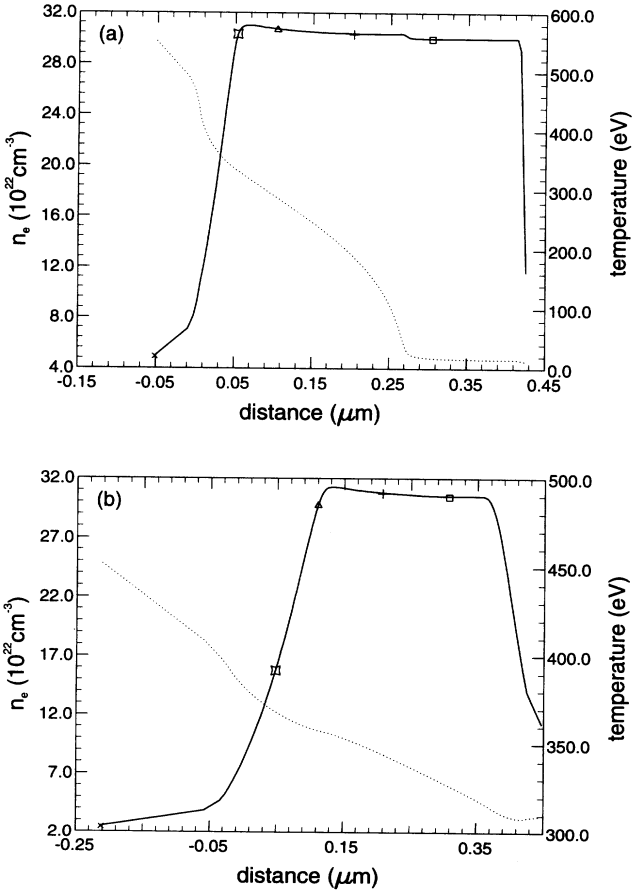


FIG. 2. The spatial profiles for (a) the density and temperature at the peak of the pulse and (b) the density and temperature at the end of the simulation. The symbols marked denote the Lagrangian cells which will be processed by the ionization dynamics model to obtain the ionization state.

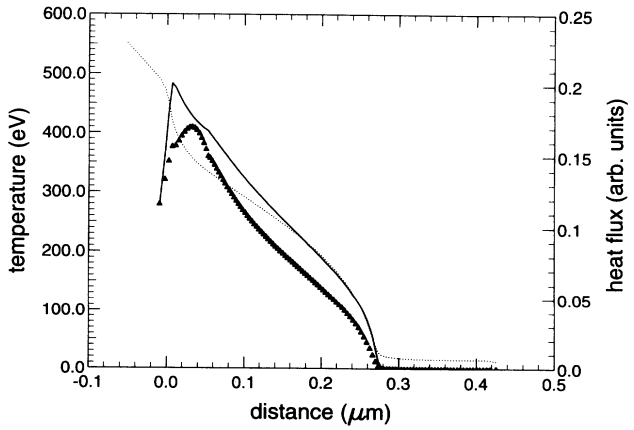


FIG. 3. The spatial profiles of the temperature (dotted line), FP heat flow (solid line), and Spitzer heat flow flux limited to 0.1 (solid triangles) at the peak of the pulse.

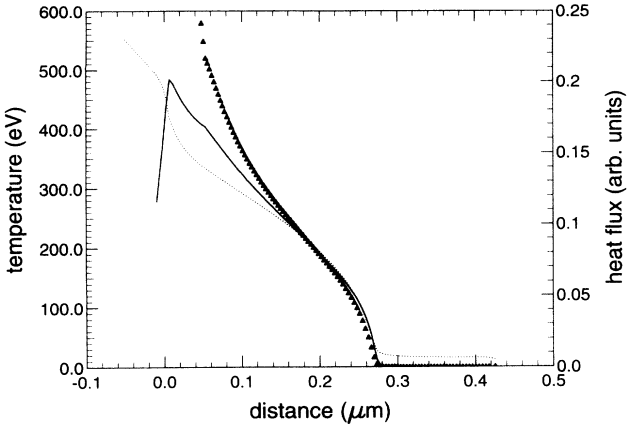


FIG. 4. The spatial profiles of the temperature (dotted line), FP heat flow (solid line), and Spitzer heat flow flux limited to 0.3 (solid triangles) at the peak of the pulse.

model is a simple convex curve, whilst the FP model has a higher region near energy absorption, but is, in general, considerably lower than the Spitzer values.

## IV. RESULTS FROM THE IONIZATION DYNAMICS MODEL

Using the ionization dynamics model we have analyzed the FP code results to obtain the ionization state of the plasma as a function of time. Using the initial conditions discussed in the preceding section we stored the density and temperature for five Lagrangian points in the target. These points are labeled with the appropriate symbols in Fig. 2.

Figure 6 plots the time evolution of the temperature and ionization state for the five Lagrangian cells. The density of the cells remains approximately constant except for the two cells closest to the laser. The outermost cell's density drops rapidly to approximately 0.5 g/cm$^3$ in 0.2 psec. The cell initially 0.05 $\mu$m into the target re-

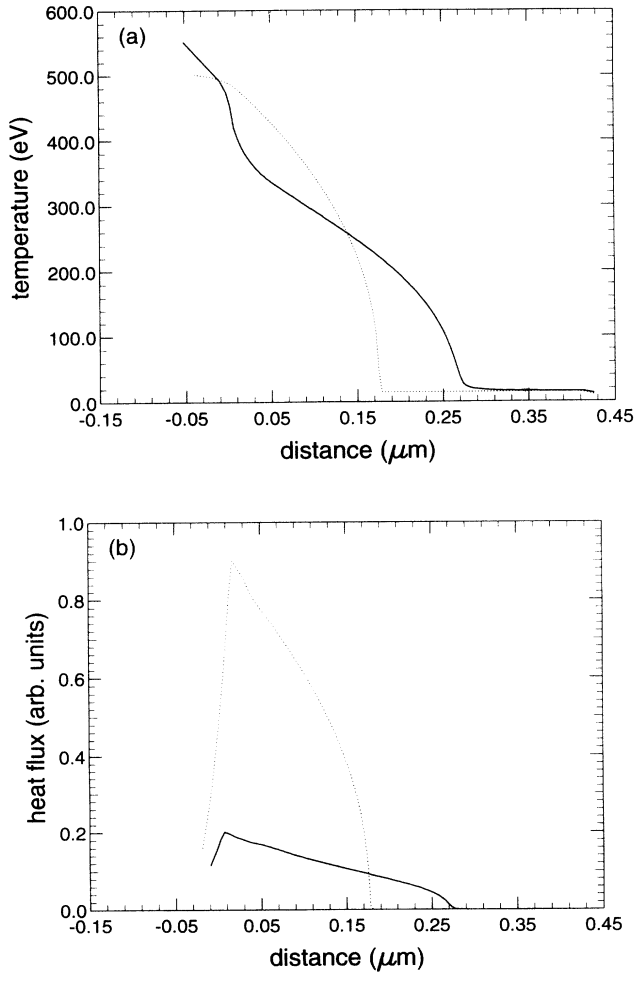


FIG. 5. Comparison between an unflux limited Spitzer hydrodynamic code (dotted line) and the FP code (solid line) at the peak of the pulse for (a) the temperature and (b) the heat flow.

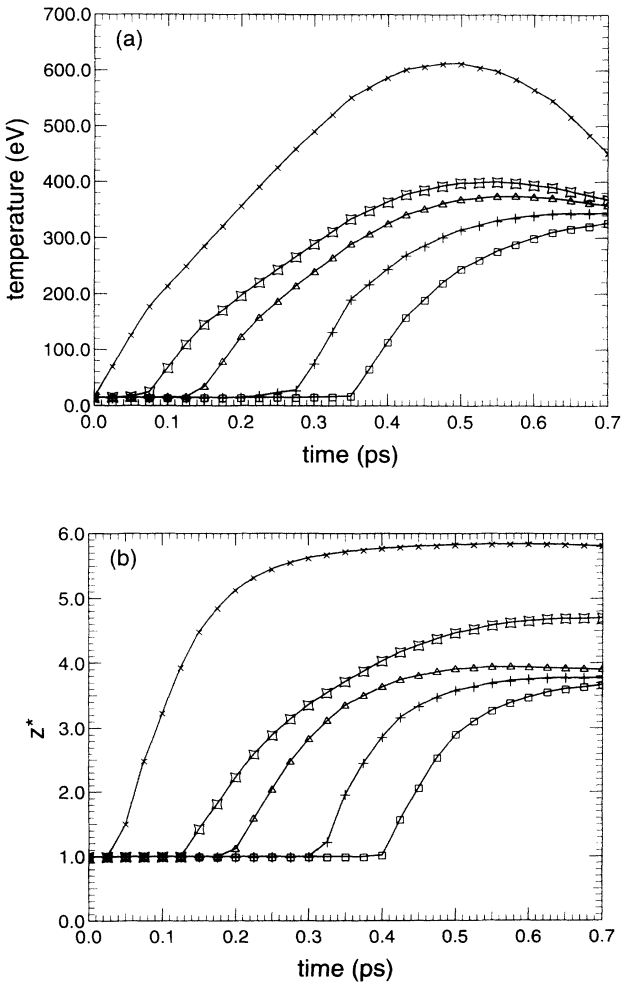


FIG. 6. The time development of (a) the temperature and (b) the average ionization state for the five Lagrangian cells marked by the appropriate symbol in Fig. 2.

mains at solid density until the peak of the pulse when it falls gradually to a density of 1.0 g/cm$^3$ by the end of the simulation. The temperature of the cell increases from 15 eV to approximately 600 eV for the cell closest to the laser. Further into the target the temperature increases as the heat front reaches the Lagrangian cell rising to approximately 300 eV by the end of the simulation. The process of ionization takes a considerable portion of the pulse. For example, the outermost cell (closest to the laser) requires 0.2 psec to reach the fully ionized state. Further into the target the carbon never reaches the fully ionized state. It should be borne in mind that we have postprocessed the data, so the energy necessary to perform ionization has not been taken into account. Hence the calculated ionization states represent the maximum possible state achievable.

To highlight the important processes involved, the ionization dynamics model was modified to allow various processes to be switched off. Figure 7 shows the average ionization state as a function of time for the outermost cell closest to the laser. We considered three cases: all processes except the radiative ones and all processes except collisional excitation and deexcitation and just collisional ionization. There was negligible differences between the state when radiative processes were ignored and the state with all terms included. The absence of all terms except collisional ionization showed a slightly faster ionization rate. The absence of collisional excitation and deexcitation marginally slowed the growth in ionization state. This slower ionization is due to the absence of stepwise ionization. When collisional excitation is included the electrons can be excited and subsequently ionized by lower velocity electrons than needed for ionization from the ground state. Hence the number of routes to ionization has been increased and thus the ionization is more rapid. All cases reached the same, fully ionized state.

Results for 0.2 $\mu$m into the target are shown in Fig. 8. Again there is no difference between the case excluding and including radiation. This is reasonable since, for the most part, the plasma is dense and relatively cold, i.e., it is a collisionally dominated plasma. The absence of collisional excitation and deexcitation decreases the rate of ionization, but does not alter the final ionization state. The absence of three-body recombination makes a substantial difference to the final ionization state and to the path of ionization. When the only process is collisional ionization the ionization state rapidly rises to $z^* = 4$, then as the heat front passes through the target the plasma ionizes further to $z^* = 6$. Three-body recombination is the inverse process of collisional ionization and through the law of detailed balance brings the ions into the correct ionization state. The region closest to the laser showed only a small difference just including collisional ionization and the presence of all terms. There is little recombining because the region is being strongly heated thus the absence of three-body recombination is negligible. However, further into the target the system is heated through conduction and never reaches full ionization; hence the absence of three-body recombination substantially alters the ionization dynamics.

For short-pulse-laser–solid interaction we can conclude that the dominant ionization mechanisms are collisional ionization and its inverse process, three-body recombination. We have also seen that the ionization process takes a significant fraction of the rise time of the pulse. However, the ionization dynamics model employs collisional and radiative rates which are formally obtained by integrating the cross section for the process over a Maxwellian distribution. In the next section we will ex-

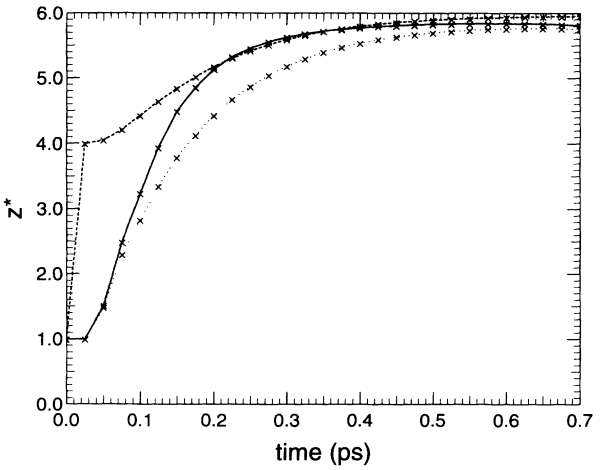


FIG. 7. The time development of the average ionization state of the outermost cell for (a) all ionization and recombination terms present (solid line), (b) radiative effects switched off (dotted line), (c) collisional excitation and deexcitation switched off (dotted line), and (d) only collisional ionization activated (dashed line). Note the line for the absence of radiative effects lies on top of the line with all terms included and is not visible.

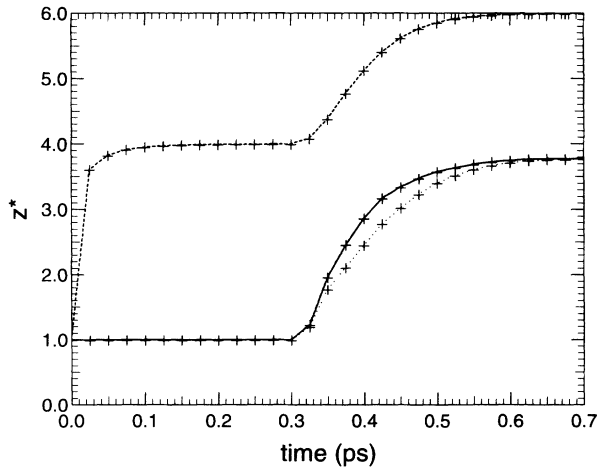


FIG. 8. The time development of the average ionization state 0.2 $\mu$m into the target for (a) all ionization and recombination terms present (solid line), (b) radiative effects switched off (dotted line), (c) collisional excitation and deexcitation switched off (dotted line), and (d) only collisional ionization activated (dashed line). Note the line for the absence of radiative effects lies on top of the line with all terms included and is not visible.

amine the effect of the non-Maxwellian character of the distribution function on the dominant collisional ionization rates.

## V. COLLISIONAL IONIZATION RATES

We have investigated the effects of the non-Maxwellian distribution function on the collisional ionization rates. This was performed by multiplying the collisional cross sections by the distribution function and integrating over all velocities then comparing the resulting rates with the rates obtained by using a Maxwellian distribution of the same density and temperature. Work performed at Belfast [18,19] has derived the collisonal ionization cross sections as a function of incident electron energy in a simple analytic form, based on the best available experimental and theoretical studies.

For certain key Lagrangian cells (as marked in Fig. 2) we output, in addition to the density and temperature, the actual distribution function and the Maxwellian distribution of the same density and temperature. We then plot the collisional ionization rate for each transition as a function of time for both the Maxwellian and non-Maxwellian distributions.

Figure 9 shows the collisional ionization rates for the outermost Lagrangian cells closest to the laser beam. The squares are the rates obtained by convolving the cross

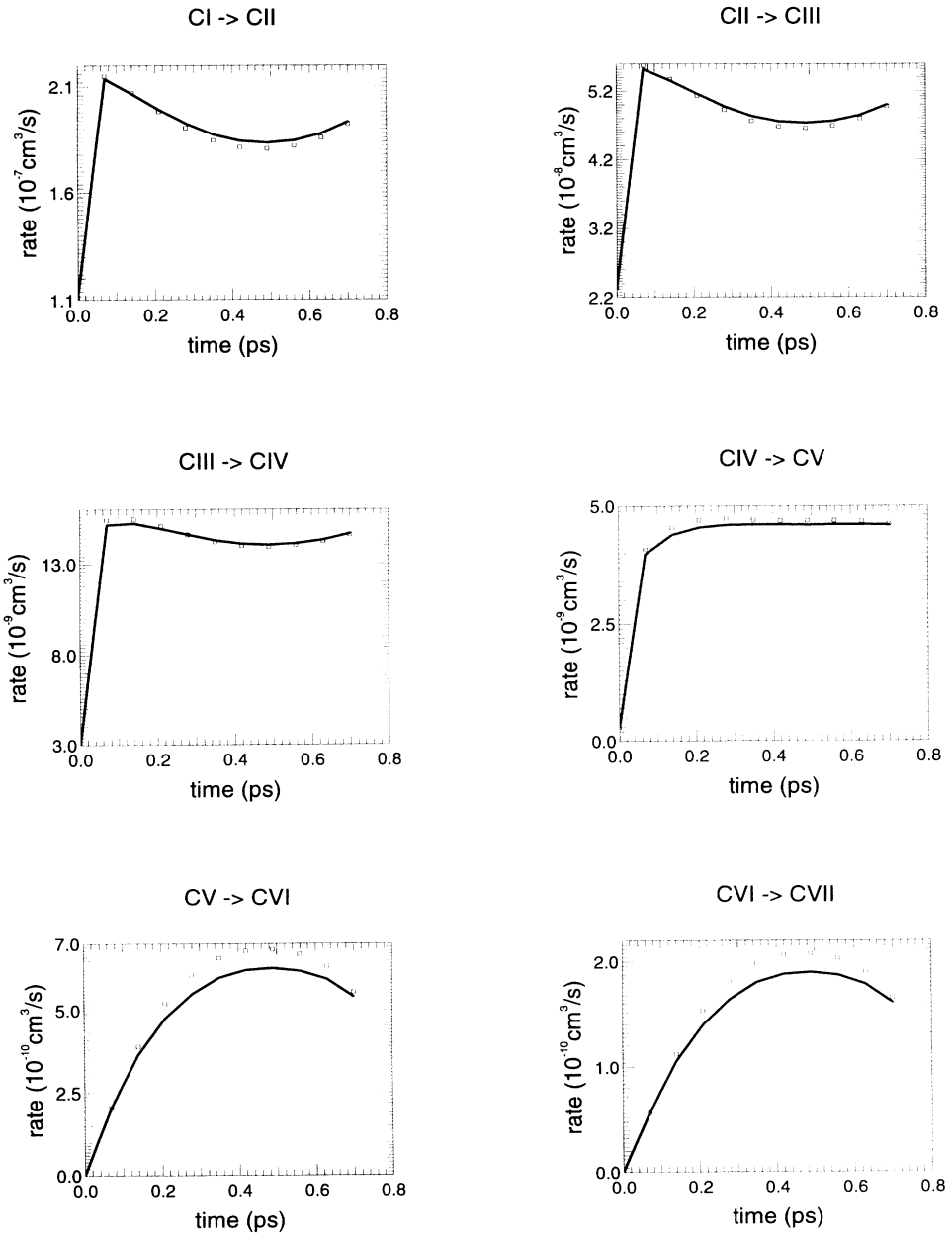


FIG. 9. The collisional ionization rates for all the ionization transitions as a function of time for the outermost cell. The squares represent the rates calculated by the actual distribution and the solid line is the rates from the Maxwellian distribution.

sections with the actual distribution whilst the solid line are those obtained from the Maxwellian distribution. As can be seen the non-Maxwellian distribution rates are very close to the Maxwellian distribution rates (at most the rates are within 5% of each other). For the low ionization transitions (up to C IV–C V) the non-Maxwellian distribution rate is below the Maxwellian distribution rate, for C V–C VI and C VI–C VII the rate for the non-Maxwellian distribution case is higher.

An examination of the distribution function and the product of the cross section multiplied by the distribution function helps to explain these results. Figure 10 shows these curves for the outermost cell at the peak of the pulse. The actual distribution function (denoted by squares) is distorted by the Langdon reduction of the low-velocity electrons. The energy of the laser is taken up by the low-velocity electrons, thus depleting this part of the distribution. When this distribution is multiplied by the

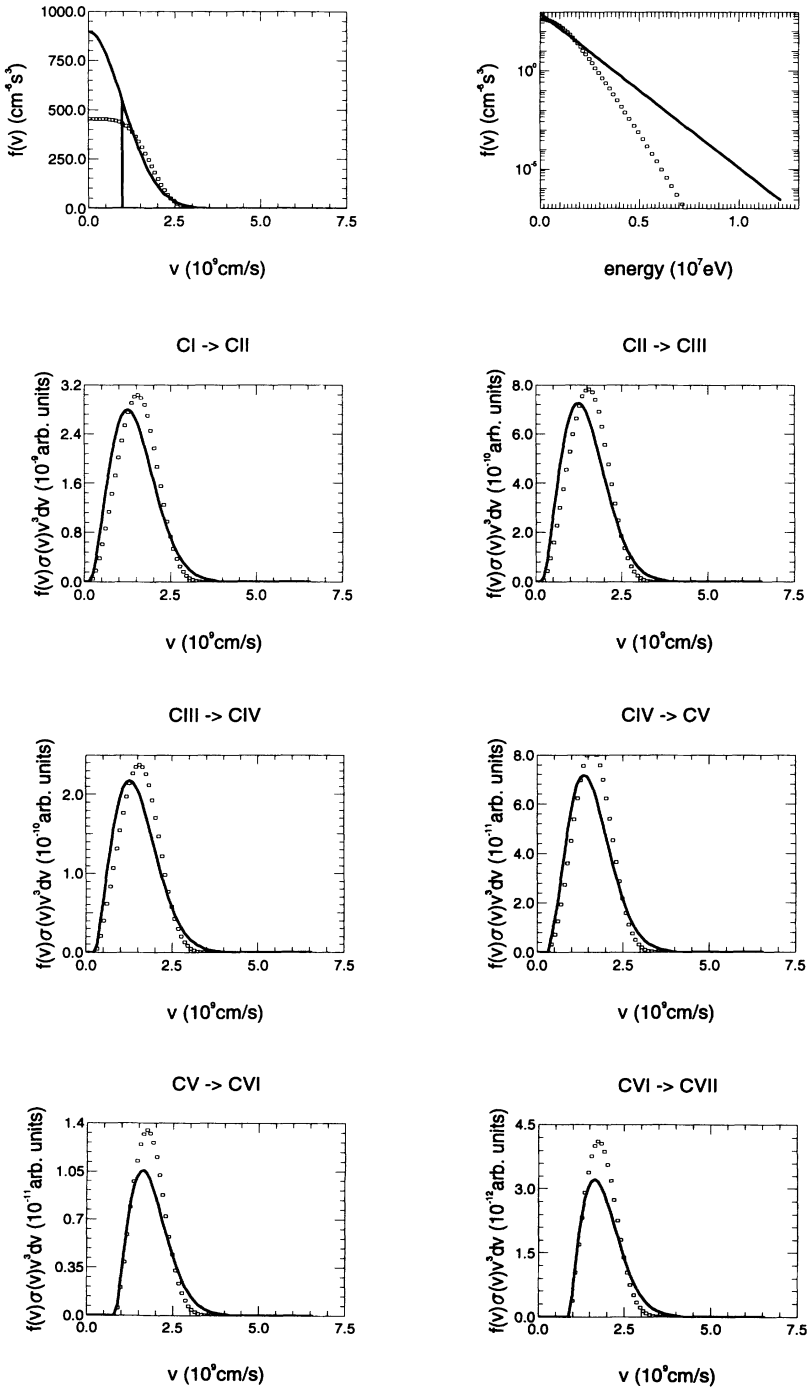


FIG. 10. The distribution function and the overlap between the cross section and the distribution function as a function of velocity for the outermost cell at the peak of the pulse. The squares represent the non-Maxwellian distribution and the solid line the Maxwellian distribution result.

cross sections the product at low velocity is lower than the Maxwellian distribution product. As the velocity increases so the Maxwellian distribution falls below the actual distribution, thus leading to the cross section product being higher for the actual distribution compared to the Maxwellian distribution. At even higher velocities the Maxwellian distribution product again dominates, but at these velocities the actual cross section is much smaller and thus contributes negligibly to the rate. The product of the cross section and distribution has the same general shape, but the peak in the non-Maxwellian distribution case is shifted to slightly higher velocities. As the ionization energy increases, so the cross-section peak shifts to higher velocity, thus moving to the region where the non-Maxwellian distribution has a larger concentration of electrons, thus increasing the rate relative to the Maxwellian distribution case. In general where the cross section is peaked in energy the distribution functions are very close.

Further into the target, for example 0.1 $\mu$m as in Fig. 11, there is practically no difference in the ionization rates. Now the only difference between the Maxwellian distribution and the actual distribution is at high velocity (see Fig. 12). At low velocities the bulk of the electrons

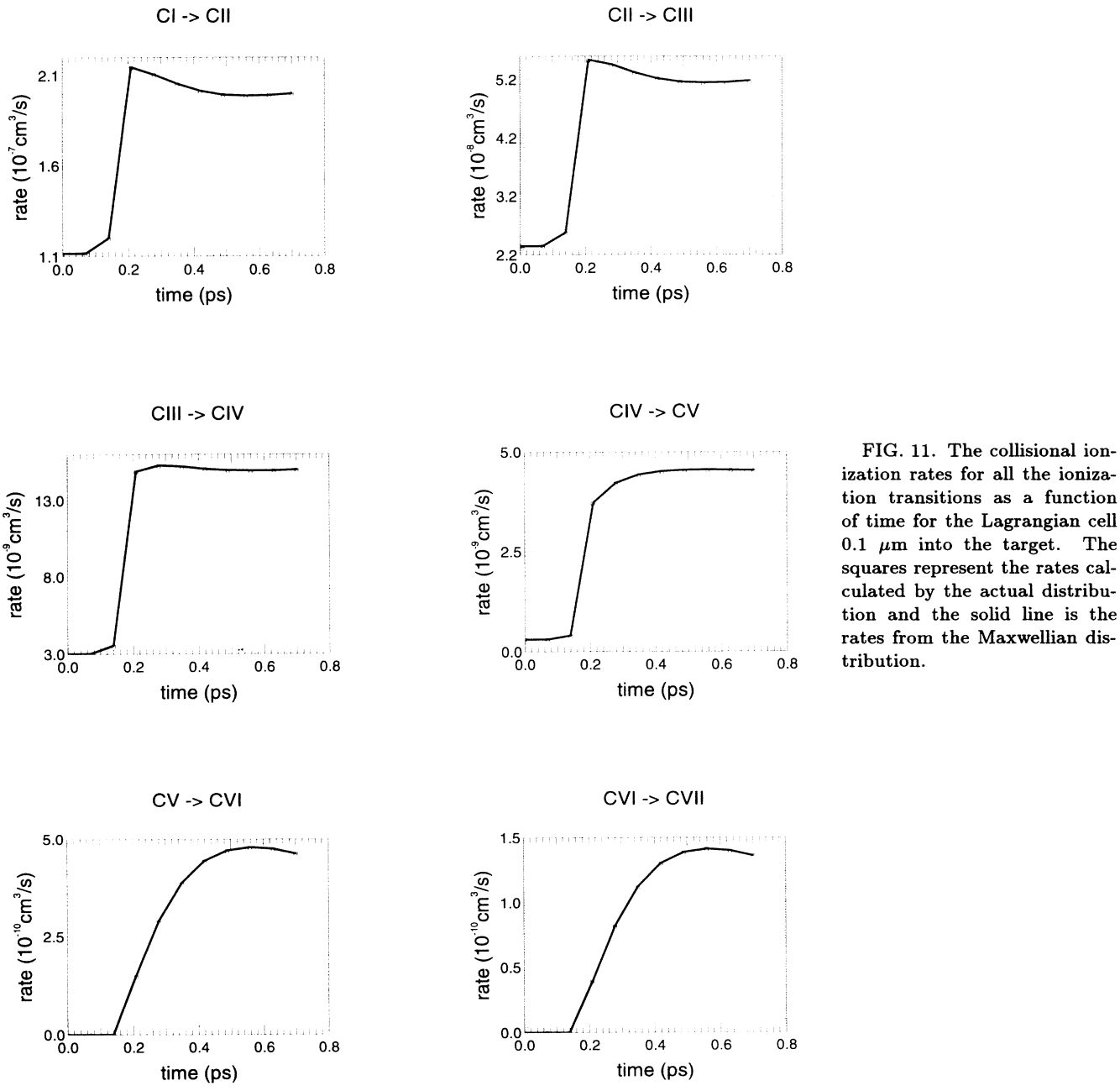


FIG. 11. The collisional ionization rates for all the ionization transitions as a function of time for the Lagrangian cell 0.1 $\mu$m into the target. The squares represent the rates calculated by the actual distribution and the solid line is the rates from the Maxwellian distribution.

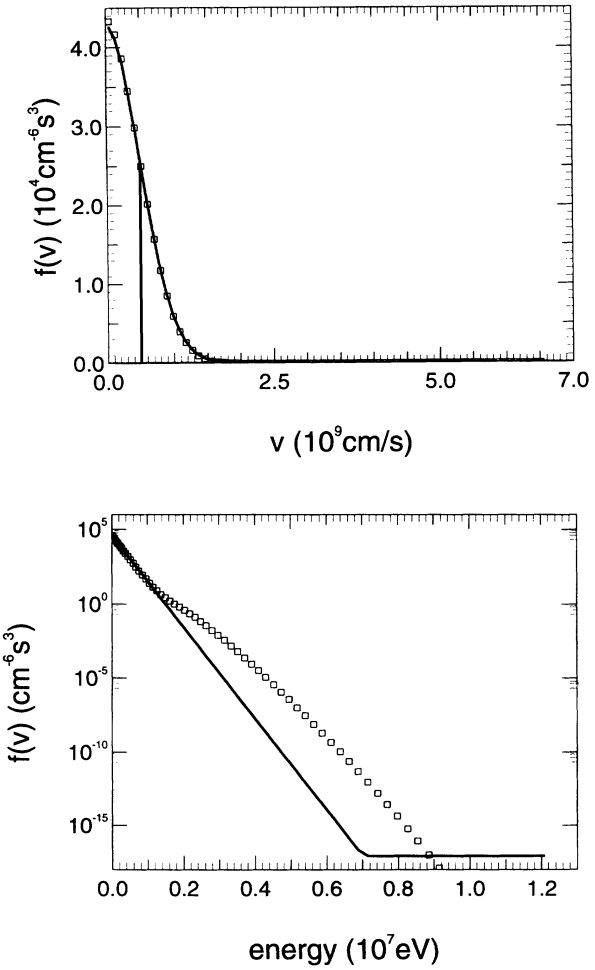


FIG. 12. The distribution function for the Lagrangian cell 0.1 $\mu$m into the target at 0.21 psec. The squares represent the non-Maxwellian distribution and the solid line the Maxwellian distribution result.

are in a Maxwellian distribution. At high velocities the tail adopts the temperature of the heated region because these are the electrons originating from that region. However, they play only a small role in determining the rate since the cross section at these velocities is typically two orders of magnitude smaller than the peak.

In summary the difference between the rates obtained using the real distribution and the rates using a Maxwellian distribution of the same density and temperature is quite small. Therefore, because of the law of detailed balance, the three-body recombination rates would also only be marginally altered by using a Maxwellian distribution rather than the actual distribution.

## VI. CONCLUSIONS

We have performed simulations using a one-dimensional FP code of the interaction of a short-pulse laser with a solid target. We have found that ion hydrodynamics cannot be ignored, even with pulse lengths as short as 350 fsec. We have shown that a single flux limit of 0.1 is too severe to model the FP heat flow in the body of the target.

By using a model of the ionization dynamics, we have postprocessed the data and found that the ionization process can take a significant fraction of the rise time of the laser pulse. We were able to identify collisional ionization and three-body recombination as the dominant ionization processes. A comparison of the rates obtained using the actual distribution and a Maxwellian of the same density and temperature was made. The differences were found to be small and justify the continued use of ionization rates based on a Maxwellian velocity distribution in simulations of these experiments.

In the future we will examine how the ionization process affects the heat flow in short-pulse-laser–solid interactions.

## ACKNOWLEDGMENTS

This work was supported by the United Kingdom's Science and Engineering Research Council and the Ministry of Defence. The authors wish to acknowledge useful discussions with K. L. Bell of The Queen's University of Belfast.

[1] L. Spitzer, Jr. and R. Harm, Phys. Rev. **89**, 977 (1953).
[2] Jie Zhang, M. H. Key, S. J. Rose, and G. J. Tallents, Phys. Rev. A **49**, 4024 (1994).
[3] A. Djaoui and S. J. Rose, J. Phys. B **25**, 2745 (1992), Appendix A.
[4] J. R. Albritton, Phys. Rev. Lett. **50**, 2078 (1983).
[5] A. R. Bell, Phys. Fluids **28**, 2007 (1985).
[6] T. H. Kho and M. G. Haines, Phys. Rev. Lett. **55**, 825 (1985).
[7] E. M. Epperlein, G. J. Rickard, and A. R. Bell, Comput. Phys. Commun. **52**, 7 (1988).
[8] J. Douglas, Num. Math. **4**, 61 (1962).
[9] E. M. Epperlein, G. J. Rickard, and A. R. Bell, Phys. Rev. Lett. **61**, 2453 (1988).
[10] G. J. Rickard, A. R. Bell, and E. M. Epperlein, Phys. Rev. Lett. **62**, 2687 (1989).
[11] E. M. Epperlein, Laser Part. Beams **12**, 257 (1994).
[12] A. B. Langdon, Phys. Rev. Lett. **44**, 575 (1980).
[13] P. Gibbon and A. R. Bell, Phys. Rev. Lett. **68**, 1535 (1992).
[14] W. A. Lokke and W. H. Grasberger, Lawrence Livermore National Laboratory Internal Report No. UCRL-52276, 1977 (unpublished).
[15] M. Chaker *et al.*, Phys. Fluids **B3**, 167 (1991).
[16] U. Teubner *et al.*, Phys. Rev. Lett. **70**, 794 (1993).
[17] P. Gibbon, in *Proceedings of the 1992 CECAM Workshop on Short Pulse Laser Plasma Interactions*, edited by M. G. Haines (Université Paris Sud, France, 1992), p. 35.
[18] K. L. Bell, H. B. Gilbody, J. G. Hughes, A. E. Kingston, and F. J. Smith, Phys. Chem. Ref. Data **12**, 891 (1983).
[19] M. A. Lennon, K. L. Bell, A. E. Gilbody, J. G. Hughes, A. E. Kingston, M. J. Murray, and F. J. Smith, Phys. Chem. Ref. Data **17**, 1285 (1988).